Ceramics International 48 (2022) 2306–2316

Contents lists available at ScienceDirect

Ceramics International

journal homepage: www.elsevier.com/locate/ceramint

Combustion synthesis and characterization of $Li_{1.2}Mn_{0.52}Ni_{0.20}Co_{0.08}O_2$ cathodes for Li-Ion battery: Effect of fuel mixture and annealing temperature

Samuel O. Ajayi, Cyril O. Ehi-Eromosele *, Kolawole O. Ajanaku

Department of Chemistry, Covenant University, PMB 1023, Ota, Nigeria

ARTICLE INFO

Keywords:
Combustion synthesis
Raman spectroscopy
Elemental analysis
Structural properties
Thermodynamics

ABSTRACT

The effect of fuel mixture and annealing temperature on the structural properties and electrochemical performance of $Li_{1.20}Mn_{0.52}Ni_{0.20}Co_{0.08}O_2$ powders prepared by the combustion synthesis were studied. Different combinations of citric acid fuel and ammonium acetate along with post-temperature treatments could be used to control the product characteristics. Simultaneous thermal analyses and thermodynamic modelling were used to describe the combustion processes. The analysis of the XRD data and other reports showed that the synthesis method and chemical compositions of lithium-rich layered oxides (LLO) could influence their description either as a solid solution or a 'composite' structure. The annealing temperature greatly influenced the lattice parameters, unit cell volumes, crystallite sizes, and cationic disorder of the samples whilst the use of fuel mixture had little effect. Furthermore, the electrochemical performances of the cathode materials were studied and the relationship with the structural properties of the powder samples were analysed. The $Li_{1.20}Mn_{0.52}Ni_{0.20}Co_{0.08}O_2$ powders synthesized with only citric acid fuel (100-T) displayed the best electrochemical performance compared with those produced using the fuel mixtures. The enhanced electrochemical performance of the 100-T cathodes was shown to be an integrative property of the highest values reported for their structural properties. The results show that citric acid assisted combustion and annealing temperature (mostly with pre-annealing) could be used to optimize the electrochemical performance of LLO cathode materials.

1. Introduction

Lithium-ion batteries (LIBs) have attracted a lot of interest as energy storage systems because of their high energy density, rechargeability, portability, and low costs. One effective way to improve the electrochemical performance of LIB is to optimize the structural properties of the cathode or anode materials. It has been shown that both the specific capacity and cycling stability of LIBs depend greatly on the electrode materials. Specifically, studies have shown that the operating redox potentials, cost of production, safety, energy density, power density and the stability of LIBs are determined by the positive electrode [1–4]. Therefore, in recent years, the pursuit of high capacity, stable and safe positive electrode is one of the most prevalent topics in material sciences. The lithium-rich layered oxides (LLOs) are considered to be one of the most promising next generation cathode materials for LIBs. Generally, the LLOs can be represented in their composite form ($xLi_2MnO_3{\cdot}(1–x)LiMO_2$) or in their solid solution form ($Li_{1+x}M_{1-x}O_2$) where M = Co, Ni, and Mn. They are very attractive due to their low cost of production, less toxicity, and can deliver very high capacities of >200 mAh/g when charged above 4.5 V [4–7]. In spite of all these advantages over other conventional cathode materials, LLOs demonstrate performance limitations such as poor initial Coulombic efficiency, poor rate capability, voltage and capacity fade that affect their practical applications.

To address these performance limitations, various approaches such as surface modification [8,9], lattice doping [10,11], core-shell structure design [12,13], nanostructure design [14], spinel structure doping [15,16], and optimization of the synthetic route [17,18] have been investigated. It is well known that the method of synthesis can be used to influence structure, morphology and particle size of synthesized materials, which in turn can affect their electrochemical performance. Synthetic routes such as sol-gel [19], mechanochemical [6,12,13], hydrothermal [20], co-precipitation [21], and combustion synthesis [22–24] have been used in synthesizing LLO cathode materials.

* Corresponding author.
E-mail address: cyril.ehi-eromosele@covenantuniversity.edu.ng (C.O. Ehi-Eromosele).

https://doi.org/10.1016/j.ceramint.2021.10.009
Received 4 July 2021; Received in revised form 13 September 2021; Accepted 3 October 2021
Available online 6 October 2021

However, combustion synthesis has proven to be a very convenient method of preparing oxides due to its simplicity, low cost of production, easy scalability, energy and time conservation [22–24].

In combustion synthesis, the product characteristics such as morphology and size can be influenced by some tunable parameters like nature and mixture of fuels, fuel-to-oxidiser ratio and subsequent annealing of the as-combusted products using variable temperatures. Even though products from combustion synthesis have a porous morphology as a result of the evolution of gases, fuels like acetate precursors have been used to produce larger amounts of gaseous by-product of the combustion reaction leading to a material with more open porous microstructures [22]. These characteristics correspondingly influence their electrochemical properties as cathode materials in LIBs. It is very important that fuels used in combustion synthesis are inexpensive, easy to handle, and with a limited environmental impact. In our previous reports on the synthesis of Li_2MnO_3 cathodes [25,26], citric acid fuel was found to produce Li_2MnO_3 cathodes with better electrochemical performance. Also, citric acid is an eco-friendly fuel and a good complexing agent since it is a polyhydroxy carboxylic acid with three carboxylic acid groups and one hydroxyl group hence it could also act as a fuel in a combustion process.

In this study, a composite $Li_{1.2}Mn_{0.52}Ni_{0.20}Co_{0.08}O_2$ (equivalently $0.5Li_2MnO_3{\bullet}0.5LiNi_{0.5}Mn_{0.3}Co_{0.2}O_2$) material is prepared by SCS using different amounts of citric acid and ammonium acetate fuel mixtures to optimize the structural properties and electrochemical performance of this cathode material. An LLO material with a very small amount of cobalt was selected. The absence of cobalt is desired in LLO materials to reduce their costs however, this can lead to a low initial discharge capacity and a poor rate performance due to cation mixing of Li^+ and Ni^{2+} ions [27]. Therefore, to achieve good electrochemical performance and to reduce cost, a small amount of cobalt is introduced into the LLO material. Furthermore, combustion synthesis can be applied to a varied range of stoichiometries and can also be used to reduce cation mixing in ceramic oxides. In addition, the as-obtained products from combustion synthesis were subjected to different annealing temperatures to further optimize their electrochemical performances.

2. Experimental section

2.1. Materials

Analytical grade $Ni(NO_3)_2{\cdot}6H_2O$ (Alfar Aesar-Puratronic ≥ 99%), $Mn(CH_3COO)_2{\cdot}4H_2O$ (Sigma-Aldrich ≥ 99%), $Co(NO_3)_2{\cdot}6H_2O$ (Sigma-Aldrich ≥ 98%), $LiNO_3$ (Suprapur ≥99%), $C_2H_7NO_2$ (Sigma-Aldrich ≥ 99%) and $C_6H_8O_7.H_2O$ (Emsure ACS), $C_2H_7NO_2$ (Sigma-Aldrich ≥ 98%) were used without further purification.

2.2. Synthesis

The $Li_{1.2}Mn_{0.52}Ni_{0.20}Co_{0.08}O_2$ cathode materials were prepared by the solution combustion synthesis (SCS) following the modified procedures adapted from other reports [28,29]. First to prepare fuel stoichiometric composition using only citric acid as fuel (i.e., 100%), 0.83 g $LiNO_3$, 1.31 g $Mn(NO_3)_2{\cdot}4H_2O$, 0.58 g $Ni(NO_3)_2{\cdot}6H_2O$, 0.23 g $Co(NO_3)_2{\cdot}6H_2O$ and 1.64 g $C_6H_8O_7{\cdot}H_2O$ were dissolved in 20 ml of distilled water and the solutions were heated to 80 °C to form a viscous gel of precursors under magnetic stirring. Secondly, the gel was transferred to a heating mantle set at 300 °C where the gel boiled, swelled, evolved some gases and ignited resulting in a powder. This auto-combusted powder was grounded and divided into three portions to be subjected to three different thermal regimes. The first portion was annealed at 1000 °C for 10 h in a muffle furnace, grounded and was named 100-T1. Subsequently, citric acid and ammonium acetate were used as mixed fuels in ratios 3:1 and 1:1, respectively to also synthesize $Li_{1.2}Mn_{0.52}Ni_{0.20}Co_{0.08}O_2$ cathode materials. The same procedures used in the synthesis of 100-T1 sample were followed except that 1.24 g citric acid ($C_6H_8O_7{\cdot}H_2O$) and 0.25 g ammonium acetate ($C_2H_7NO_2$) were used for the preparation of 7525-T1 while 0.82 g $C_6H_8O_7{\cdot}H_2O$ and 0.49 g $C_2H_7NO_2$ were used in the synthesis of 5050-T1 sample. It is important to note that in the mixture of fuels synthetic routes, 75% and 50% of the stoichiometric amount of citric acid, 25% and 50% of the stoichiometric amount of ammonium acetate fuels required for the complete combustion process were used instead for the preparation of 7525-T1 and 5050-T1 samples, respectively. The second portions of the auto-combusted powders obtained above were pre-annealed (500 °C/3hr) before annealing at 1000 °C for another 3hr and the samples were cooled, grounded and were denoted 100-T2, 7525-T2, and 5050-T2 samples. The third portions of the auto-combusted powders were annealed at 900 °C for 3hr after pre-annealing (500 °C/3hr) and were named 100-T3, 7525-T3, and 5050-T3 samples. All the samples were heated and cooled slowly at a rate of 2 °C min^{-1}.

2.3. Characterisation methods

The gels obtained from drying the various precursor solutions (i.e., metal nitrates and fuels) were subjected to thermal analyses - thermogravimetric and differential scanning calorimetric analyses (TG-DSC) over a range of 30–1000 °C at a heating rate of 3 °C/min in air using Netzsch Jupiter 449 C. The quantitative elemental compositions of the synthesized $Li_{1.2}Mn_{0.52}Ni_{0.20}Co_{0.08}O_2$ powders were measured by inductively coupled plasma optical emission spectroscopy (ICP-OES, iCAP 7600DUO from ThermoFisher Scientific). The crystal structure and phase composition of the synthesized materials were determined by powder X-ray diffraction (XRD) using a STOE STADI MP diffractometer. The powder samples were loaded in 0.5 mm diameter glass capillaries with diffraction patterns collected in a transmission geometry using a Mo K_α radiation ($\lambda = 0.709320$ Å) and a MYTHEN 1 K detector operated with a step width of 0.015° in the 2θ range of 3°–50°. Structural modelling in reciprocal space of the XRD data were performed by the Rietveld method using the FullProf programme. The local structure of the powder samples were studied by Raman spectroscopy using Horiba LabRam Evolution HR microscope equipped with a 632 nm HeNe solid-state excitation laser (17 mW), a 100× objective, and a 600 grooves per millimeter grating. The morphology of the synthesized materials were examined by SEM/EDS (Zeiss Merlin GEMINI 2).

2.4. Electrochemical measurements

The charge-discharge tests were performed using the CR2032 coin cell which is made up of a cathode and lithium metal anode separated by a Celgard 2325 separators. The cathode electrode was prepared from a mixture of 80 wt% active material (synthesized $Li_{1.2}Mn_{0.52}Ni_{0.20}Co_{0.08}O_2$ materials), 10 wt% carbon black (TIMCAL Super C65) and 10 wt% polyvinylidene fluoride binder (Solvay Solef 6020) in 1-methyl-2-pyrrolidone (Merck EMPLURA) with continuous magnetic stirring for about 4 h. The resulting slurry was pressed onto an aluminium foil and dried at 80 °C overnight in a vacuum oven. This electrode film was cut into a disc with 12 mm diameter and used as the working electrode. The CR2032 coin cells were assembled in a glovebox (MBraun) under argon atmosphere. The electrolyte used is LP30 selectylite (BASF) electrolyte which consists of 1 M $LiPF_6$ in ethylene carbonate/dimethyl carbonate (EC/DMC, 1:1 v/v). Electrochemical measurements of the assembled coin cells were done using different constant current densities between 2.0 and 4.8 V in a VMP3 multi-channel potentiostat (Biologic, France) at 25 °C. Also, Electrochemical Impedance spectra (EIS) measurements were carried out to analyze the ionic conductivity of the material by measuring the impedance the material presents in response to an external applied AC potential. These measurements were obtained between 1 Hz and 1 MHz with a 10 mV amplitude AC signal.

3. Results

3.1. Thermodynamics of the combustion syntheses of $Li_{1.2}Mn_{0.52}Ni_{0.2}Co_{0.08}O_2$

In combustion synthesis, the textural and structural properties of the synthesized materials such as crystallite size, size distribution, crystallinity and even cation disorder are dependent on the enthalpy or flame temperature produced during the combustion reaction. This enthalpy of the combustion reaction which also determines the porosity (through the volume of evolved gases) of the material can be primarily controlled by the nature of fuel and the fuel-to-oxidiser ratio. The amount of fuel(s) required in the redox mixture (with the metal nitrates) for the combustion reactions was calculated based on stoichiometric composition. The stoichiometric composition is the ratio at which oxygen content of oxidizer can be reacted to consume fuel entirely and no heat exchange is required for the complete reaction. Concerning the nature of fuel, the different compositions of citric acid and ammonium acetate will present different combustion flame temperatures for the syntheses of $Li_{1.2}Mn_{0.52}Ni_{0.2}Co_{0.08}O_2$ materials. Calculations based on a simplified thermodynamic approach have been used to model the relative exothermicity of the combustion processes mediated by the different compositions of citric acid and ammonium acetate fuels. These calculations have been carried out to predict the combustion conditions such as the enthalpy of formation of the $Li_{1.2}Mn_{0.52}Ni_{0.2}Co_{0.08}O_2$ powders, and the amount of gases produced during combustion.

The thermodynamic stoichiometric equation for the complete combustion reaction using different compositions of citric acid and ammonium acetate fuels are presented in equations (1)–(3).

100% Citric acid fuel (100-T samples):

$$1.20LiNO_3 + 0.52Mn(NO_3)_2{\cdot}4H_2O + 0.20Ni(NO_3)_2{\cdot}6H_2O + 0.08Co(NO_3)_2{\cdot}6H_2O + 0.78C_6H_{10}O_8 \rightarrow \mathbf{Li_{1.2}Mn_{0.52}Ni_{0.2}Co_{0.08}O_2} + 4.68CO_2\uparrow + 7.66H_2O\uparrow + 1.40N_2\uparrow \quad (1)$$

75% Citric acid and 25% Ammonium acetate fuels (7525-T samples):

$$1.20LiNO_3 + 0.52Mn(NO_3)_2{\cdot}4H_2O + 0.20Ni(NO_3)_2{\cdot}6H_2O + 0.08Co(NO_3)_2{\cdot}6H_2O + 0.59C_6H_{10}O_8 + 0.32C_2H_7NO_2 \rightarrow \mathbf{Li_{1.2}Mn_{0.52}Ni_{0.2}Co_{0.08}O_2} + 4.18CO_2\uparrow + 7.83H_2O\uparrow + 1.56N_2\uparrow \quad (2)$$

50% Citric acid and 50% Ammonium acetate fuels (5050-T samples):

$$1.20LiNO_3 + 0.52Mn(NO_3)_2{\cdot}4H_2O + 0.20Ni(NO_3)_2{\cdot}6H_2O + 0.08Co(NO_3)_2{\cdot}6H_2O + 0.39C_6H_{10}O_8 + 0.64C_2H_7NO_2 \rightarrow \mathbf{Li_{1.2}Mn_{0.52}Ni_{0.2}Co_{0.08}O_2} + 3.62CO_2\uparrow + 7.95H_2O\uparrow + 1.72N_2\uparrow . \quad (3)$$

It was observed that the viscous gel of the precursor solutions of 100-T and 7525-T compositions after drying at 80 °C turned pink while that of 5050-T turned purple. The pink colouration of the gels is probably due to the citric acid since 100-T composition with the highest amount of citric acid displayed a deeper pink colour. After the combustion reaction, 100-T gel turned into a brownish powder while those of 7525-T and 5050-T turned into black powders.

Using relevant thermodynamic data for the reactants and products [30] of the combustion reactions (as shown in Table S1 in the supplementary information), the enthalpy of the combustion reactions were calculated using equation (4) assuming complete combustion reactions as presented in equations (1)–(3). The enthalpy of formation for $Li_{1.2}Mn_{0.52}Ni_{0.2}Co_{0.08}O_2$ is set at zero due to the lack of its thermodynamic data and moreover, $Li_{1.2}Mn_{0.52}Ni_{0.2}Co_{0.08}O_2$ is constant for all the combustion reactions.

$$nH_{combustion} = \left(\sum nnH_f\right)_{products} - \left(\sum nnH_f\right)_{reactants} \quad (4)$$

Where, $\Delta H_{combustion}$ is the enthalpy of the combustion reaction, n is the number of moles, and ΔH_f is the heat of formation.

The effect of the nature of fuel on the heat of formation of product ($nH_{combustion}$), and the amount of gases produced during combustion reaction are shown in Table 1. The $nH_{combustion}$ for the combustion reactions were close. However, the 100% citric acid fuel (100-T composition) assisted SCS produced the highest $nH_{combustion}$ (−1493.81 kJ/mol) while the 5050-T composition produced the least $nH_{combustion}$ (−1354.61 kJ/mol). The results imply that the exothermicity of the combustion reaction reduced as the quantity of citric acid reduced and that of ammonium acetate was increased. The $nH_{combustion}$ can influence the crystallinity of the synthesized $Li_{1.2}Mn_{0.52}Ni_{0.2}Co_{0.08}O_2$ materials. Also, the amounts of gases produced from the combustion reactions as obtained from equations (1)–(3) are very close. Following the same trend with the $nH_{combustion}$, the 100-T composition produced the highest while the 5050-T produced the least amounts of gases. However, more gas evolution was observed for the 7525-T and 5050-T compositions during the combustion process compared to the 100-T sample. This could be attributed to the addition of ammonium acetate which can produce large amounts of gaseous by-products during the combustion reaction. These gaseous decomposition products includes intermediates such as nitrogen oxides, ammonia, and HNCO [29].

3.2. Thermal analysis of the combustion processes

Simultaneous TGA-DSC analyses of the precursor gels (mixtures of metal nitrates and fuels) of the 100-T, 7525-T, and 5050-T compositions for the preparation of $Li_{1.2}Mn_{0.52}Ni_{0.2}0Co_{0.08}O_2$ were undertaken to study the effect of the fuel compositions and heat treatment on the combustion reactions. The TGA-DSC curves of the precursor gels for 100-T, 7525-T, and 5050-T compositions are given in Fig. 1. Mass losses in the TGA curves of the 100-T, 7525-T, and 5050-T compositions are observed to be about 10%, 18%, and 23% corresponding to their first DSC exothermic peaks at about 230 °C, 225 °C and 218 °C, respectively. These mass losses are due to complete evaporation of water and organic contents in the precursor gels. The amount of weight loss shown by the various compositions corresponds to the amount of fuel (organic content) in the precursor gels which can be seen from the fuel-to-oxidiser molar ratio (Table 1) of the various compositions. The 5050-T had the highest fuel-to-oxidiser molar ratio (0.52) while the 100-T had the least (0.39). Subsequently, large mass losses (~58% for 100-T, ~51% for 7525-T, and 40% for 5050-T) were recorded in the TGA curves which corresponded to the sharp exothermic peaks (~345 °C for 100-T, ~301 °C for 7525-T, and ~283 °C for 5050-T) seen in the DSC curves. These sharp exothermic peaks indicates the decomposition of the metal nitrates-fuels dried gel during the combustion reaction. It can be seen that the 100-T recorded this largest mass loss while the 5050-T showed the lowest. These mass losses corresponds to the enthalpy of the combustion reaction (Table 1) in which the 100-T gave the highest (−1493.81 kJ/mol) while the 5050-T gave the lowest (−1354.61 kJ/mol). Unlike other reports [29,31], the composition with the highest value of heat of combustion (i.e. 100-T) required the highest temperature (~345 °C) for the combustion reaction in this study. Also, as reported earlier, the 100-T (compared to the other compositions) required the highest temperature (~230 °C) that corresponded with the first mass loss seen in the TGA curves. These results show that a fuel with a higher value of heat of combustion will give a higher temperature of exothermic decomposition compared to a fuel with a lower heat of

Table 1
Effect of the nature of fuel on the heat of formation of product ($nH_{combustion}$), and the amount of gases produced during combustion reaction.

Sample	Fuel-to-oxidiser molar ratio	$nH_{combustion}$ (kJ/mol)	Amount of gas produced (mole)
100-T	0.39	−1493.81	13.74
7525-T	0.46	−1434.34	13.57
5050-T	0.52	−1354.61	13.29

Note: The enthalpy of formation for $Li_{1.2}Mn_{0.52}Ni_{0.2}Co_{0.08}O_2$ is set at zero.

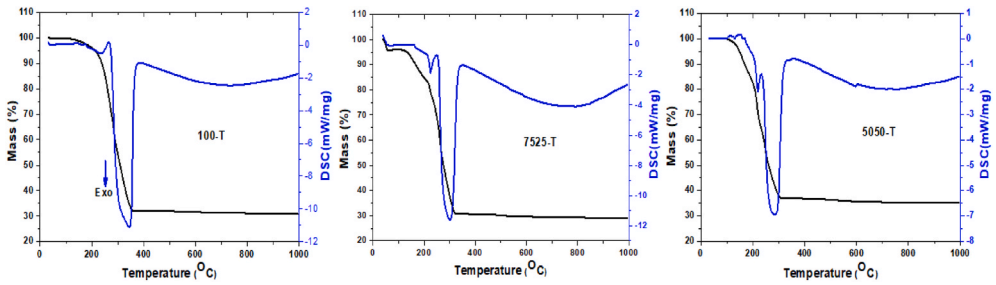

Fig. 1. TG-DSC curves of the precursor gels (mixtures of metal nitrates and fuels) of the 100-T, 7525-T, and 5050-T compositions for the preparation of $Li_{1.2}Mn_{0.52}Ni_{0.2}0Co_{0.08}O_2$.

combustion value. Overall, the 5050-T recorded the least weight loss compared to the other compositions which is consistent with their $nH_{combustion}$.

It can be seen that no further weight loss is observed for all the compositions after the combustion reactions giving products that are free of residual reactants and carbonaceous matter. Also, this shows that the crystalline $Li_{1.2}Mn_{0.52}Ni_{0.2}0Co_{0.08}O_2$ material has already been formed around this temperature [32]. The TGA-DSC results describes the combustion processes and corroborates their thermodynamic considerations. In addition, it shows that the nature of fuel influences the combustion synthesis of $Li_{1.2}Mn_{0.52}$ $Ni_{0.2}0Co_{0.08}O_2$.

3.3. Elemental analysis

The average metal compositions of the synthesized $Li_{1.2}Mn_{0.52}$-$Ni_{0.2}Co_{0.08}O_2$ materials were determined by inductively coupled plasma - optical emission spectrometry (ICP-OES) and the results are shown in Table 2. All samples gave varied metal compositions compared to the target (nominal) composition. Compared to the samples synthesized using a mixture of fuels (i.e., 5050-T and 7525-T series), the samples synthesized with only citric acid fuel (100-T) had the highest amounts of Li, total metal content (Li + M) and ratio of the amount of Li to transition metals (Li/M), irrespective of the annealing temperature used during syntheses. For example, 100-T1 with a Li/M content of 1.377 is higher than that of 7525-T1 (1.362) and 5050-T1 (1.357). These results show that the part substitution of citric acid fuel with ammonium acetate used in the combustion synthesis reduced the complexing ability of citric acid which led to the loss of more metals as seen in the 5050-T and 7525-T samples compared to the 100-T samples. Also, a reduced annealing temperature aided higher amounts of Li + M contents in the samples irrespective of the nature of fuel used. The 100-T3, 7525-T3, and 5050-T3 samples (annealed at 900 °C/3hr after pre-annealing at 500 °C/3hr) had Li + M contents of 2.014, 1.990, and 2.006, respectively. Conversely, 100-T1, 7525-T1, and 5050-T1 samples annealed at a higher annealing temperature and duration (1000 °C/10hr) had lesser Li + M contents of 1.949, 1.932, and 1.928, respectively. It can be seen that the nature of fuel and annealing temperature affected the stoichiometry of the samples.

Table 2
Elemental analysis of the synthesized $Li_{1.2}Mn_{0.52}Ni_{0.2}Co_{0.08}O_2$ powders using ICP-OES.

Sample	Li	Transition metals, M			M	Li + M	Li/M
		Mn	Ni	Co			
Target composition	1.200	0.520	0.200	0.080	0.800	2.000	1.500
100-T1	1.129	0.541	0.199	0.080	0.820	1.949	1.377
7525-T1	1.114	0.538	0.199	0.081	0.818	1.932	1.362
5050-T1	1.110	0.538	0.200	0.080	0.818	1.928	1.357
100-T2	1.166	0.510	0.193	0.077	0.780	1.946	1.495
7525-T2	1.156	0.517	0.193	0.077	0.787	1.943	1.469
5050-T2	1.167	0.521	0.195	0.078	0.794	1.961	1.470
100-T3	1.253	0.499	0.185	0.077	0.761	2.014	1.647
7525-T3	1.226	0.503	0.187	0.074	0.764	1.990	1.605
5050-T3	1.244	0.500	0.187	0.075	0.762	2.006	1.633

Furthermore, the elemental analysis results show that at higher annealing temperature (irrespective of the nature of fuel used), the amounts of Li reduced significantly while the amounts of the transition metals where higher compared to the target metal composition. For example, 100-T1 gave Li amounts of 1.129 while 100-T3 showed higher Li content of 1.253. Conversely, 100-T1 gave higher transition metals content (0.820) while 100-T3 displayed lesser amount (0.761). It is well known that Li loss is associated with annealing hence at a higher annealing temperature, more Li loss is recorded as seen in -T1 samples compared to a lesser temperature annealed -T3 samples. Interestingly, in addition, the gain of higher amounts of Li in –T3 samples invariably resulted in lesser amounts of the total transition metals in the samples when compared to the target stoichiometry. The effect of adding excess Li, to compensate for Li loss during annealing, on the amounts of transition metals in LLO and NCM layered oxides have to be further investigated.

3.4. Structural characterization of the $Li_{1.20}Mn_{0.52}Ni_{0.20}Co_{0.08}O_2$ powder samples

3.4.1. XRD analysis

The XRD profiles of the $Li_{1.20}Mn_{0.52}Ni_{0.20}Co_{0.08}O_2$ powder samples prepared by SCS using different amounts of citric acid and ammonium acetate fuel mixtures coupled with annealing at varying temperatures are given in Fig. 2. The samples gave XRD patterns characteristic of a LLO material which can be indexed to the monoclinic system with the C2/m space group [33,34]. All the XRD peaks are quite narrow and sharp with no visible impure phase present. It can be seen that all the samples have a well-crystalline layered structure and show a clear splitting of the 13-3 and 33-1 peaks (see the indexed diffraction patterns of the 7525-T1 sample in Fig. 2). The XRD data of the samples were analysed using the Rietveld refinements by FullProf suite and the lattice parameters and other crystallographic data obtained are given in Table 3. Firstly, Rietveld refinements were applied to the XRD data assuming a 'composite' material consisting of two integrated phases with C2/m and R3m space group symmetry [5,6,12,35] but gave poor fits for the data. Secondly, a structural model consisting only the R3m space group (α-$NaFeO_2$ structure) was used for the refinements [36] but it also gave poor fits for the data. It is important to state that there is an ongoing debate on the structure of the LLO material whether it is a solid solution or a 'composite' material. Interestingly, our group have synthesized this same LLO material ($Li_{1.2}Mn_{0.52}Ni_{0.20}Co_{0.08}O_2$) by mechanically alloying the already prepared components (i.e. $0.5Li_2MnO_3$ and $0.5LiNi_{0.5}Mn_{0.3}Co_{0.2}O_2$) to form the LLO nanocomposite. This LLO nanocomposite was well refined by a model consisting of two phases (C2/m and R3m space group) indicating a 'composite' material [6,12]. However, using a combined XRD and transmission electron microscopy (TEM) analysis, it has been shown that LLO material is a single-phase solid solution with C2/m monoclinic symmetry and not a 'composite'

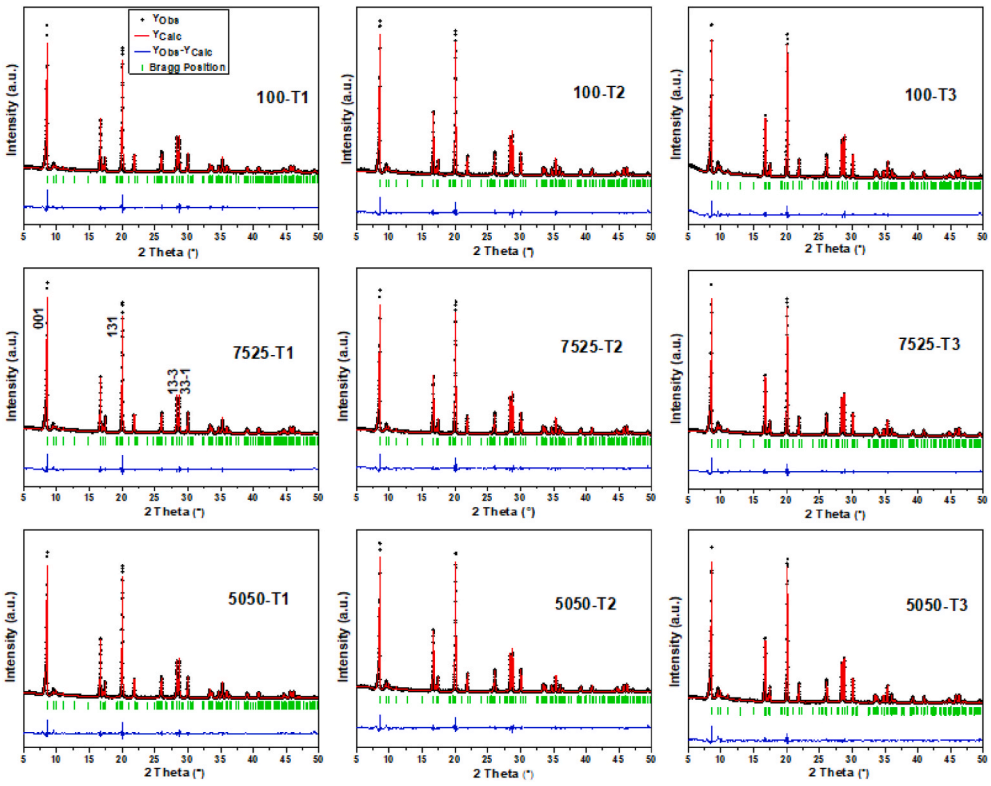

Fig. 2. Experimental XRD patterns and the Rietveld refinements of pristine 100-T1, 7525-T1, 5050-T1, 100-T2, 7525-T2, 5050-T2, 100-T3, 7525-T3, and 5050-T3 powders. The black dots represents the experimental pattern; red line is the calculated pattern; blue line is the difference between experimental and calculated patterns; green ticks represent the Bragg reflection positions of monoclinic Li_2MnO_3 phase (i.e. C2/m space group). (For interpretation of the references to colour in this figure legend, the reader is referred to the Web version of this article.)

Table 3
The lattice parameters and other crystallographic data obtained from the Rietveld refinement of the XRD data for $Li_{1.20}Mn_{0.52}Ni_{0.20}Co_{0.08}O_2$ powder samples.

Samples	100- T1	7525-T1	5050-T1	100- T2	7525-T2	5050-T2	100-T3	7525-T3	5050-T3
Annealing conditions	1000 °C/10 h			500 °C/3 h and 1000 °C/3hr			500 °C/3 h and 900 °C/3 h		
a (Å)	4.954 (1)	4.955 (4)	4.954 (1)	4.944 (5)	4.944 (7)	4.942 (7)	4.934 (6)	4.937 (4)	4.936 (5)
b (Å)	8.568 (2)	8.571 (6)	8.572 (2)	8.558 (2)	8.558 (4)	8.556 (2)	8.539 (1)	8.547 (1)	8.546 (2)
c (Å)	5.036 (1)	5.037 (8)	5.037 (9)	5.030 (3)	5.030 (8)	5.029 (4)	5.021 (5)	5.025 (7)	5.024 (8)
β (°)	109.31 (2)	109.30 (5)	109.31 (3)	109.21 (1)	109.30 (1)	109.29 (1)	109.28 (2)	109.29 (2)	109.29 (1)
V (Å^3)	201.69 (1)	201.92 (6)	201.85 (7)	200.84 (6)	200.83 (6)	200.71 (4)	199.68 (3)	200.15 (6)	200.02 (3)
FWHM (001) peak (°)	0.0792	0.0762	0.0809	0.0812	0.0788	0.0812	0.0836	0.0801	0.0794
Crystallite size (nm)[b]	46.34	48.16	45.34	45.18	46.56	45.17	43.90	45.80	46.21
I_{001}/I_{131}[c]	1.18	1.15	1.10	1.07	1.09	1.07	1.07	1.10	1.08
OccMn2b (%)[d]	67.80	68.32	69.06	64.61	62.95	62.64	59.57	59.72	55.18
R_{wp} (%)	9.78	8.21	8.98	8.72	8.79	9.43	7.53	7.68	8.56
χ^2 (%)	3.77	2.97	2.97	2.85	2.55	2.78	2.64	2.67	3.25

[a]The numbers in parentheses are the estimated standard deviations of the last significant figure.
[b] The crystallites sizes are obtained from the full width-at-half maximum (FWHM) of the 001 peak using Scherrer equation.
[c] The intensity ratio of the 001 and 131 peaks in the XRD patterns.
[d] OccMn2b describes the refined amount of Mn on the 2b-site (i.e., Li site in the TM-layer).

material [33,34]. Correspondingly, the single-phase solid solution with the C2/m space group gave better fit for the XRD data obtained in this study. Other reports [5,34] and our previous studies on same material [6,12] suggest that the synthesis method and chemical compositions of LLO materials could influence whether the LLO can be described based on the solid solution or a 'composite' structure.

The lattice parameters obtained from the Rietveld refinement of the XRD data are given in Table 3 along other crystallographic data obtained from the XRD analysis. Apart from the lattice parameters and profile shape parameters, the site occupancies (i.e. Li–Mn disorder between 2b and 4 g sites) along with the atomic positions in the C2/m Li_2MnO_3 monoclinic symmetry were refined. It is important to note that Mn in this structural symmetry here also represents other transition metals such as Ni and Co present in the LLO material since they are substituted for Mn. Other micro-structural parameters such as isotropic size and strain were not refined because of the inability of the FullProf program to model this complex nanocomposite C2/m structure [5]. The reliability factors (R_{wp} and χ^2) shows a good fit of the structural model with the raw data as seen in Fig. 2. There was a noticeable decrease in the lattice parameters of the samples with decrease in annealing temperature/duration which can be seen from the reduced unit cell volumes from -T1 to -T3 samples. For example, the unit cell volume of 100-T1, 100-T2, and 100-T3 samples are 201.69, 200.84, and 199.68 Å^3, respectively. Other reports have shown that increased annealing temperature increases the unit cell volume of LLO materials [16,37]. As expected, the same trend is seen with this influence of annealing temperature on the crystallite sizes of the materials as shown in Table 3. The crystallite sizes of 100-T1, 100-T2, and 100-T3 samples are 46.34, 45.18, and 43.90 nm, respectively. The full-width-at-half-maximum (FWHM) values were used in the calculation of the crystallite sizes according to the Scherrer equation and it can be seen that they have an inverse relationship with the crystallite sizes i.e., the lesser the FWHM

values, the higher the crystallite size of the materials and vice-versa. In the same heat treatment regime, the results show that the change of the type/amount of fuel used had virtually no effect on the a, b, and c lattice parameters of the samples. For example, the a lattice parameters of 100-T1, 7525-T1, and 5050-T1 are 4.954, 4.955, and 4.954 Å, respectively. In the same manner, no trend was seen in the effect of fuel on the crystallite sizes when the same heat treatment was applied to the synthesized materials.

Furthermore, the peak intensity ratio (I_{001}/I_{131}) for all the samples are given in Table 3. It is generally used to evaluate the degree of cation disorder in LLO materials in which a higher I_{001}/I_{131} value means lesser cation disorder. Generally, it is reported that a I_{001}/I_{131} value less than 1.2 is indicative of cationic disorder in the materials [32,38]. Apart from the 100-T1 and 7525-T1 samples with a I_{001}/I_{131} value of ~1.2, other samples gave values of ~1.10 showing invariance with annealing temperature. It is expected that the samples prepared using the highest temperature treatments such as the –T1 samples will have the least cation disorder as also shown in other reports [16]. The OccMn2b values which gives the refined amount of Mn-occupation on the 2b site has also been used to describe cation disorder in LLO materials [16,25]. Surprisingly, the OccMn2b values decreased with reducing annealing temperature for the samples suggestive of reduced cation disorder. For example, the OccMn2b values of 100-T1, 100-T2, and 100-T3 are 67.80%, 64.61%, and 59.57%, respectively. Notwithstanding, it is possible that OccMn2b values also describes other crystallographic parameters other than cation disorder. It has been reported that OccMn2b might be an indicator for a fine dispersion of the C2/m and R3m phases (solid solution) and low Li_2MnO_3 domain thickness in the LLO material [5]. Also, it has been shown that increase in the firing temperature can increase the layered phase structure of the LLO material [16]. These analyses seem to agree with the OccMn2b values which decreased with reduced annealing temperature for these samples suggesting a better solid solution/finely dispersed nanocomposite for the –T1 samples compared to the –T3 samples. Generally, the analyses of the XRD results show that whilst the annealing temperature had significant effect on the structural parameters, the fuel mixture route adopted in this study had lesser effect on the structural parameters of the synthesized materials.

3.4.2. *Raman spectroscopy analysis*

Raman spectroscopy of the synthesized $Li_{1.20}Mn_{0.52}Ni_{0.20}Co_{0.08}O_2$ powder samples were done to further evaluate the microstructural changes in these materials since this method has been shown to be more sensitive to short-range ordering compared to XRD [39]. Fig. 3 shows the Raman spectra of $Li_{1.20}Mn_{0.52}Ni_{0.20}Co_{0.08}O_2$ powder samples synthesized using different fuel mixtures (a) and annealing temperature (b). The Raman spectra of all samples are characteristic of LLO materials [6]. Typically, the Raman spectra of LLO contains two major peaks corresponding to the stretching A_{1g} and bending E_g modes of transition metals-oxygen bonds. Furthermore, in Li_2MnO_3 (a parent compound of the LLO), these two dominant peaks are assigned to phonon vibrations with the A_g mode due to the vibrations of the Mn atoms along the b-axis while the B_g mode (i.e. E_g mode) is associated with the vibrations of Li atoms in the Mn layer (i.e. along the a- and c-axis) [40].

In our previous work on Li_2MnO_3 [25], we have analysed the crystallite sizes of Li_2MnO_3 from the peak width of the A_g mode with Raman peak broadening (W) correlated with a reduction in crystallite size. It can be seen from Fig. 3a that 100-T1 sample had the smallest A_g peak broadening (W = 73 cm^{-1}) while the 5050-T1 sample had the least (W = 77 cm^{-1}). This means that the 100-T1 sample gave the highest crystallite size while the 5050-T1 sample had the least even though the difference is expected to be small as a result of their close W values. Unlike in the XRD analysis, these crystallite size analysis from Raman spectra broadening agrees with the reaction conditions calculated from the thermodynamic considerations in which the 100-T condition produced the highest exothermicity and heat absorbed by the $Li_{1.20}Mn_{0.52}Ni_{0.20}Co_{0.08}O_2$ product while the 5050-T condition produced the least. It is well known that the higher the synthesis temperature for ceramic oxide materials, the higher the crystallite size. In Fig. 3b, the W values of 100-T samples annealed at different temperatures present significant differences. The 100-T1 sample (W = 73 cm^{-1}) gives the highest crystallite size while the 100-T3 sample (W = 122 cm^{-1}) had the least in agreement with the crystallite sizes calculated from XRD data (see Table 3).

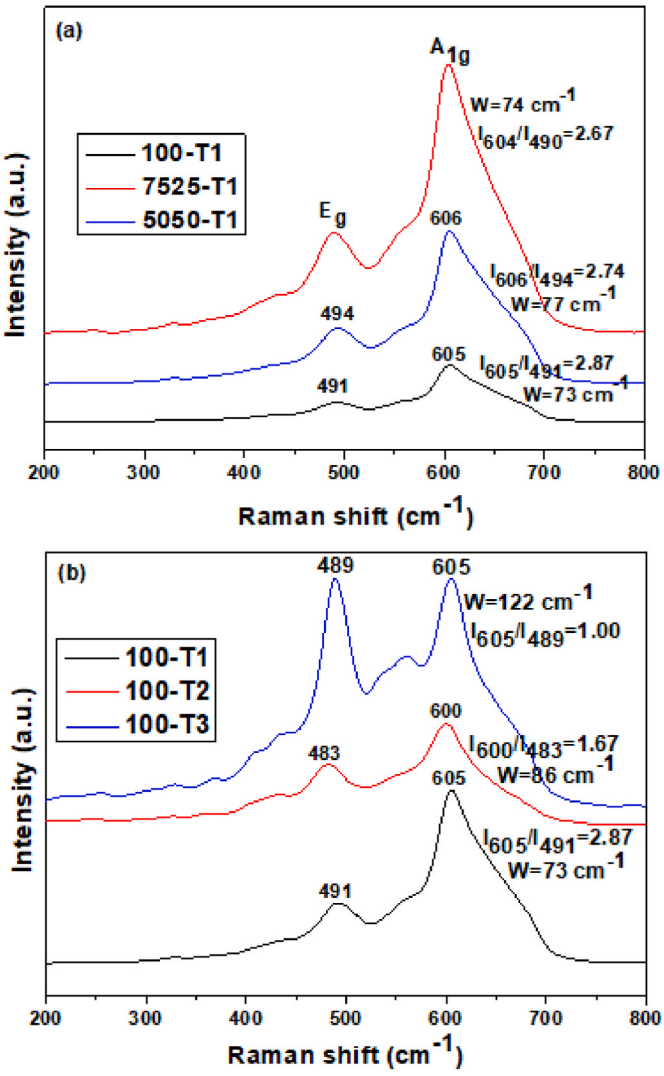

Fig. 3. Raman spectra of $Li_{1.20}Mn_{0.52}Ni_{0.20}Co_{0.08}O_2$ powder samples synthesized using different fuel mixtures (a) and annealing temperature (b).

In addition, the ratio of the absolute intensities of the two most intense Raman peaks (I_{A1g}/I_{Eg}) have been correlated with cationic disorder in the transition metal layer with a higher I_{A1g}/I_{Eg} indicating a lesser cationic disorder [25]. The 100-T1 sample gave the highest I_{A1g}/I_{Eg} (I_{605}/I_{491} = 2.87) while the 7525-T1 sample gave the least (I_{604}/I_{490} = 2.67) as shown in Fig. 3a. This means that the 100-T1 sample gave the least cationic disorder like in the XRD analysis. In Fig. 3b, there is a significant variation of I_{A1g}/I_{Eg} with annealing temperature. Whilst, the 100-T1 sample annealed at the highest temperature showed the highest I_{A1g}/I_{Eg} (I_{605}/I_{491} = 2.87), the 100-T3 sample annealed with the least temperature presented the lowest I_{A1g}/I_{Eg} (I_{605}/I_{483} = 1.00). Fig. S1 (supplementary information) gives the Raman spectra of $Li_{1.20}Mn_{0.52}Ni_{0.20}Co_{0.08}O_2$ powder samples synthesized using different fuel mixtures: (a) annealed at 1000 °C/3hr (-T2) and (b) annealed at 900 °C/3hr (-T3). The same trends explained here concerning the influence of fuel and annealing temperature on the

crystallite size and cationic disorder were also observed for the –T2 and –T3 samples. The results show that the –T3 samples presented the highest cationic disorder and most likely the poorest crystallinity since they were annealed at the lowest temperature. Unlike in the XRD analysis of the I_{001}/I_{131} peaks, the analyses of the Raman spectra I_{A1g}/I_{Eg} peaks of the samples describe well the cationic disorder in these LLO materials as expected from the influence of annealing temperature on cationic disorder. This reinforces the advantage of the Raman spectroscopy over XRD in analyzing short-range ordering in ceramic materials hence they should be used complementarily. The Raman spectra analyses show that while the type of fuel used in the SCS of $Li_{1.20}Mn_{0.52}Ni_{0.20}Co_{0.08}O_2$ samples slightly affected its crystallite size and cationic disorder, the annealing temperature markedly affected these properties.

3.5. SEM analysis of the synthesized $Li_{1.20}Mn_{0.52}Ni_{0.20}Co_{0.08}O_2$ powder materials

Fig. 4 shows the SEM images of the synthesized $Li_{1.20}Mn_{0.52}Ni_{0.20}Co_{0.08}O_2$ powder materials. The images of all the samples show agglomerated particles that are generally dense. The –T1 samples gave well developed faceted particles that had smooth surfaces and irregular shapes. Concerning the influence of fuel on the morphologies of the samples, (see –T1 samples, for example), the 5050-T1 sample showed the largest particle sizes distribution while the 100-T1 sample gave the least. This suggests that the 5050 fuel condition (i.e. having the highest amount of ammonium acetate) increased the agglomeration of primary particles resulting in large secondary particles. Also, the annealing temperature affected the morphologies of the samples. The -T1 samples gave the most developed particles while the –T2 samples gave the poorest developed particles with rough surfaces irrespective of the fuel used. Furthermore, it can be seen that the -T1 samples displayed larger particle sizes compared to their corresponding -T3 samples. Fig. 5 gives the SEM image of 7525-T2 powder and the corresponding EDS mapping showing the homogeneous distribution of Co, Ni, and Mn elements in the material.

Figure S2 (supplementary information) shows the SEM images of $Li_{1.20}Mn_{0.52}Ni_{0.20}Co_{0.08}O_2$ powder samples captured at lower magnification (1000×). At this much lower magnification, a porous structure with interconnected micro pore structures which is characteristic of combustion ceramic oxides is observed for all samples. Unexpectedly, the 5050 fuel composition (with the highest amount of ammonium acetate) didn't show any apparent higher porous structure compared to the other fuel compositions. Instead, the images show that the 100-T and 7525-T samples gave more noticeable micro pore structures. Furthermore, the micro pore structures were retained irrespective of the annealing temperature.

3.6. Electrochemical performance

Looking at the foregoing thermodynamics, thermal, elemental, and structural analyses of the $Li_{1.20}Mn_{0.52}Ni_{0.20}Co_{0.08}O_2$ powder materials, the –T1 and the –T3 samples generally presented the highest and the least values of these analyses, respectively. Therefore, we selected –T1 and –T3 samples for electrochemical testing and evaluated how the annealing temperature and nature of fuel used in their combustion synthesis affect their electrochemical behaviour. The initial charge-discharge profiles of –T1 cathodes vs Li^+/Li and their corresponding cycling performances measured at a constant current density of 10 mA/g between 2.0 and 4.8 V are shown in Fig. 6a and b, respectively. All the –T1 cathodes show the characteristic profiles of LLO cathode during the initial charge, which consists of a sloping region below 4.5 V corresponding to Li^+ deintercalation from the $LiMO_2$ component, and a plateau region above 4.5 V due to the activation of the Li_2MnO_3 component with an irreversible loss of Li_2O. As shown in Fig. 6a, the 100-TI, 7525-T1, and 5050-T1 cathodes give an initial charge capacity of 309, 268, and 402 mAh/g, while they give an initial discharge capacity of 192, 151, and 196 mAh/g, respectively. It can be seen that the

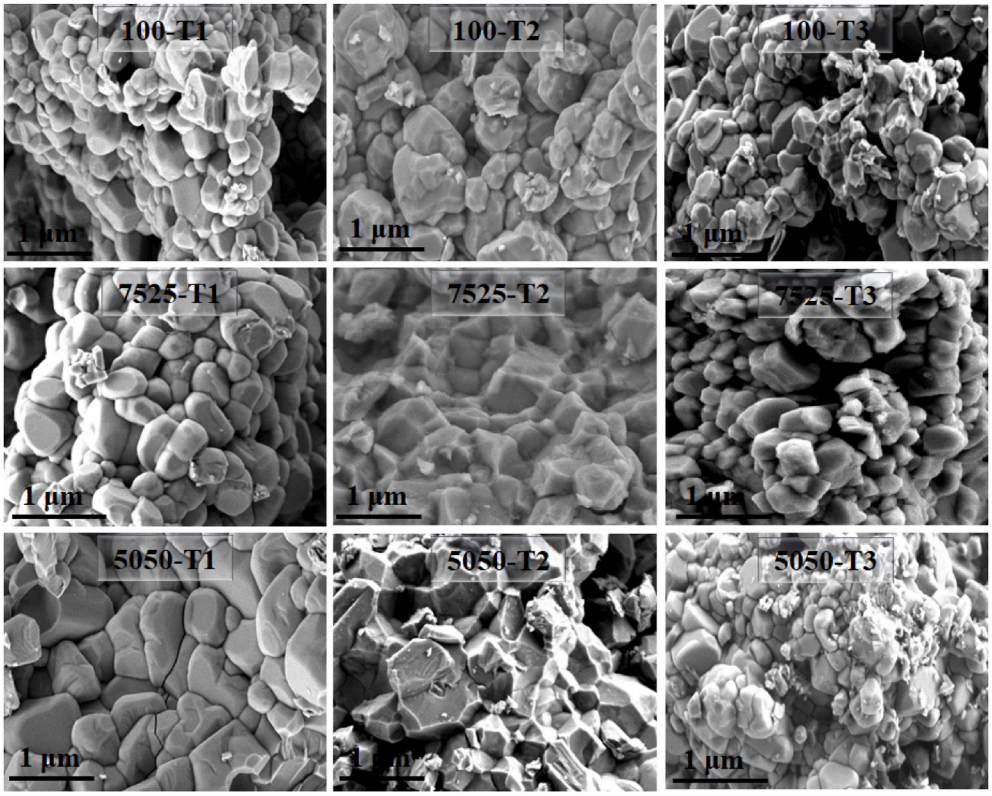

Fig. 4. SEM images of $Li_{1.20}Mn_{0.52}Ni_{0.20}Co_{0.08}O_2$ powder samples.

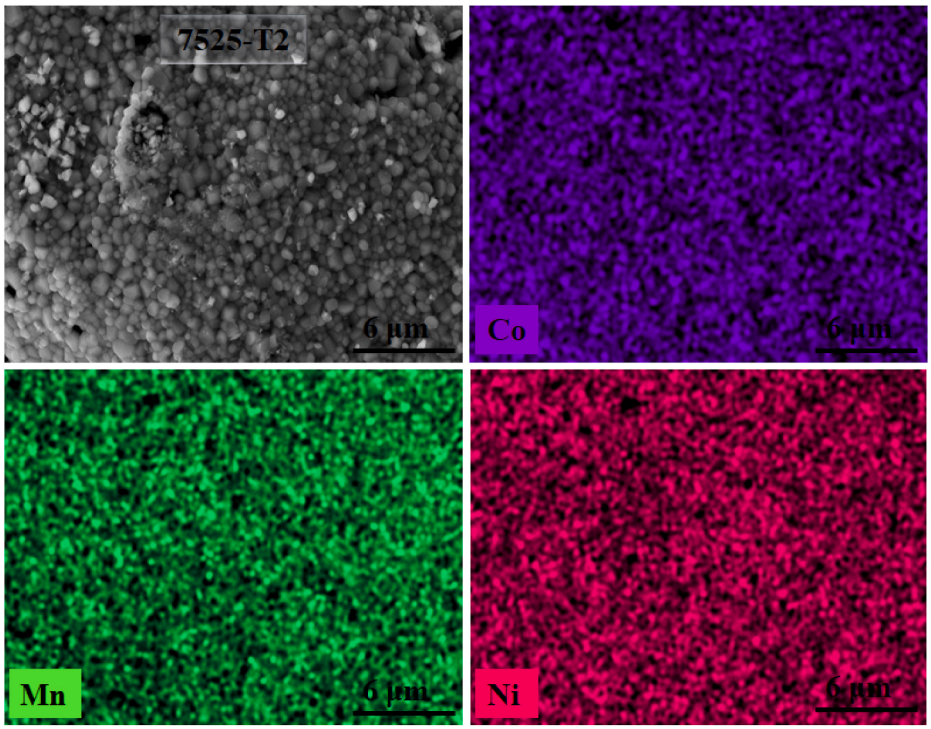

Fig. 5. SEM image of 7525-T2 powder and the corresponding EDS mapping showing the distribution of Co, Ni, and Mn elements in the material.

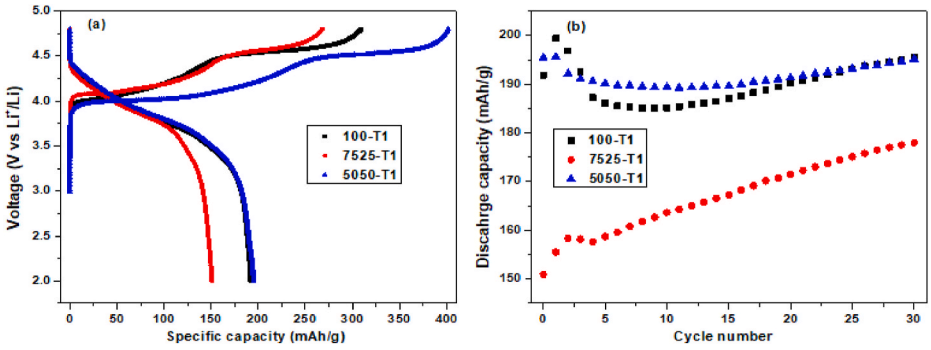

Fig. 6. Initial charge-discharge curves of –T1 cathodes vs Li^+/Li (a) and their cycling performances (b). The cells were cycled over a voltage range of 2.0–4.8 V at a rate of 10 mA g^{-1} and at 25 °C.

100-TI, 7525-T1, and 5050-T1 cathodes showed irreversible capacity loss (IRC) of 117, 117, and 206 mAh/g, respectively. However, the Coulombic Efficiency of the first cycle for the 100-TI, 7525-T1, and 5050-T1 cathodes are 62%, 56%, and 47%, respectively. The unusually high initial charge capacity observed for 5050-T1 cathode, resulting in the high IRC, could be attributed to side reactions in the cell [41]. In Fig. 6b, the 100-T1 and 5050-T1 cathodes gave comparable cycling performance with capacity fade for about 10 cycles before their

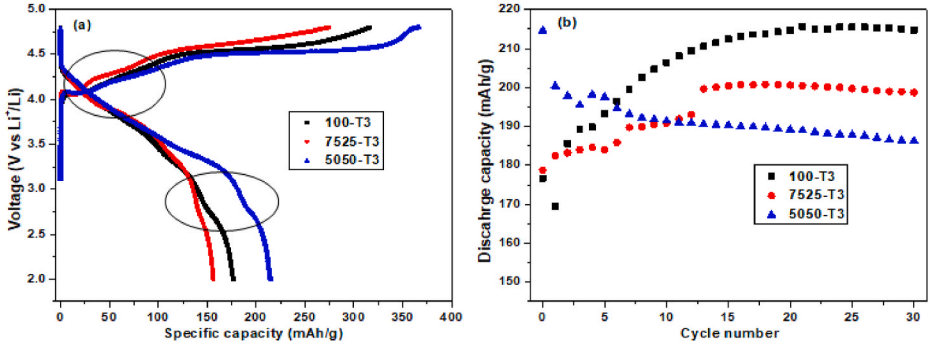

Fig. 7. Initial charge-discharge curves of –T3 cathodes vs Li^+/Li (a) and their cycling performances (b). The cells were cycled over a voltage range of 2.0–4.8 V at a rate of 10 mA g^{-1} and at 25 °C.

capacities increased slightly till the 30th cycle. The 7525-T1 cathode show lesser capacities over 30 cycles compared to the 100-T1 and 5050-T1 cathodes. However, the 7525-T1 cathode show a slow activation resulting in a steady increase of its capacity with cycling. It can be seen that the fuel used in SCS of $Li_{1.20}Mn_{0.52}Ni_{0.20}Co_{0.08}O_2$ powders affected their initial charge-discharge capacities and cycling performances.

The initial charge-discharge profiles of –T3 cathodes vs Li^+/Li and their corresponding cycling performances measured at a constant current density of 10 mA/g between 2.0 and 4.8 V are shown in Fig. 7a and b, respectively. The –T3 cathodes show the same profiles like the –T1 cathodes, but curves can be seen both in the sloping regions (indicated by circles) of the charge and discharge profiles of all the cathodes. These can be due to structural changes occurring in the cathode materials. As shown in Fig. 7a, the 100-T3, 7525-T3, and 5050-T3 cathodes give an initial charge capacity of 317, 275, and 367 mAh/g while they give an initial discharge capacity of 177, 156, and 215 mAh/g, respectively. It can be seen that the 100-T3, 7525-T3, and 5050-T3 cathodes showed IRC of 140, 119, and 152 mAh/g in the first cycle while their corresponding Coulombic Efficiencies are 56%, 34%, and 59%, respectively. Except for 5050-T3 cathode, the 100-T3 and 7525-T3 cathodes gave higher IRC and lesser Coulombic efficiencies compared to their –T1 analogues. However, as also recorded with the 5050–T1 cathode, the 5050-T3 cathode gave the highest IRC compared to other cathodes. The cycling performances of the –T3 cathodes (Fig. 7b) show that the 5050-T3 cathode which recorded the highest initial discharge capacity (215 mAh/g) suffered from a capacity fading to 180 mAh/g after 30 cycles. Apart from the side reactions occurring between the electrode materials and electrolyte solution, capacity fading is also known to originate from the layered-spinel phase transformation which is a major drawback in the commercialization of LLO cathode materials. The 100-T3 and 7525-T3 cathodes with an initial discharge capacity of 177 and 156 mAh/g showed a steady capacity increase to 215 and 199 mAh/g, respectively. This steady capacity increase is due to the gradual activation of Li_2MnO_3 component in the 100-T3 and 7525-T3 cathodes which was already completed at the initial cycle in the 5050-T3 cathode. It can be seen that the annealing temperature affected the electrochemical performances of the $Li_{1.20}Mn_{0.52}Ni_{0.20}Co_{0.08}O_2$ cathodes looking at their initial capacities and cycling performances. Furthermore, in the highest annealing temperature (-T1), 100-T1 and 5050-T1 both gave a capacity retention of about 100% after 30 cycles while in the lowest annealing temperature (-T3), 100-T3 and 5050-T3 showed a capacity retention of 122% and 87%, respectively. The electrochemical test results show that the 100-T cathodes gave the best electrochemical performance compared to the 7525-T and 5050-T cathodes.

To understand the electrochemical performance of these cathodes as shown above, electrochemical impedance spectroscopy (EIS) of selected cathodes were undertaken. The Nyquist plots obtained from EIS data for the 5050-T1, 7525-T1, and 7525-T3 cathodes measured prior to cycling and after 10 cycles are shown in Fig. S3. It can be seen that the Nyquist plots consists of semicircles at high frequency region which is due to charge transfer resistance (Rct) and a 'long tail' in the low frequency region related to the Li-ion diffusion behaviour in the cathode material. It is evident that the semicircles of the cathodes (see the inset diagrams) prior to cycling are larger than after 10 cycles indicating a reduction in Rct with cycling. This reduction in Rct with cycling (after 10 cycles) may be responsible for the steady increase of the capacity of these cathodes as seen in their cycling performance. The pristine 5050-T1 cathode gives a smaller Rct than the pristine 7525-T1 cathode resulting in its higher capacity as recorded in the cycling performance. The 7525-T3 pristine cathode which gave similar Rct with the 7525-T1 pristine cathode (see Fig. S3a), displayed a higher Rct after 10 cycles. The EIS results show that the nature of fuel and the annealing temperature influenced the kinetic properties of the electrodes resulting in the differences seen in their electrochemical performances.

4. Discussion

4.1. The influence of the structural properties of $Li_{1.20}Mn_{0.52}Ni_{0.20}Co_{0.08}O_2$ powders on their electrochemical performances

It is well known that the capacity and cyclic performance of LIBs depend on the composition, morphology, and crystal structure of the electrode materials. These parameters, as has been shown in this study, are dependent on synthesis method and post-treatments applied to the material. The elemental analyses show that the 100-T samples had both higher Li and Li + M contents than the 7525-T and 5050-T samples. Also, the results show that the 100-T3 sample had the highest Li + M contents compared to both the 100-T1 and 100-T2 samples (see Table 2). Generally, the larger the Li + M contents, the higher the energy density since Li + M represents the intercalated ion and redox-active elements, respectively. However, the initial discharge capacity and cycling performance of the cathodes can't be explained singly from the Li + M contents in the materials. For example, the 100-T1 and 5050-T1 cathodes presented similar electrochemical performance while the 5050-T3 cathode with a higher Li + M contents (2.006) compared to the 5050-T1 cathode (1.928) showed poorer cycling stability.

Many reports have shown the effect of crystallite and particles sizes of cathode materials on their electrochemistry [25,42]. Generally, smaller particle sizes exhibits higher capacity in the initial stage but with a larger tendency for capacity fade. Bigger particle sizes with relatively lower capacity in the initial stage tend to have an increasing capacity with cycling. The SEM results show that the 100-T1 sample had smaller particles than the 5050-T1 sample even though it presented slightly higher crystallite sizes (Table 3). However, the 100-T1 and 5050-T1 cathodes presented similar electrochemical performance. Also, the –T1 samples clearly showed higher crystallite sizes and particles sizes than the –T3 samples from the XRD and SEM analyses. The cycling performance of 100-T1 cathode displayed capacity fade for about 10 cycles before its capacity increased slightly. In comparison, the 100-T3 cathode with a lesser initial capacity show an increasing capacity with cycling therefore displaying a better capacity retention. In addition, the 5050-T3 with even a higher initial capacity compared to the 5050-T1 cathode showed capacity fading and a poorer capacity retention. It is clear from these results that their electrochemical performance can't be explained singly from their crystallite/particle sizes.

Furthermore, the Raman scattering analysis showed that the –T1 samples had far lesser cationic disorder compared to the –T3 samples. High cationic disorder is usually associated with poorer crystalline materials and has been reported to block Li^+ intercalation/deintercalation in cathode materials thereby resulting in high IRC [43]. Recall that the initial charge-discharge profiles of the –T3 cathodes (Fig. 7a) showed structural changes (indicated by circles) which might be due to their poorer crystallinity. This might also be responsible for their generally lower Coulombic efficiencies and IRC compared to the –T1 cathodes. This assertion is supported by the higher Rct after 10 cycles for the 7525-T3 cathode compared to the 7525-T1 cathode. Poor crystallinity could result in kinetic limitations of Li^+ intercalation/deintercalation in the –T3 cathodes manifesting as capacity fade seen in the 5050-T3 cathode and the delayed activation of Li_2MnO_3 component in the 100-T3 cathode. In addition, it is known that the enlargement of lattice parameter 'c' and crystallite volume facilitate Li^+ intercalation/deintercalation. Table 3 shows that the –T1 samples had larger lattice parameter 'c' and crystallite volume than the –T3. It is possible that the higher lattice parameter 'c' and crystallite volume of the –T1 samples may have also contributed to their better electrochemical performances compared to the –T3 samples. Suffice to state that no direct correlation/trend of any of the structural properties of the materials with their electrochemical performances could be established. It is well known that the cyclic performance of a material is an integrative parameter affected by crystallite size, chemical composition, particle morphology, crystallinity, etc. In this regard, the 100-T cathodes

with the highest amounts of Li, transition metals and crystallite size, least cationic disorder, and good crystallinity gave the best electrochemical performance compared to the 7525-T and 5050-T cathodes.

5. Conclusions

The combustion synthesis of $Li_{1.20}Mn_{0.52}Ni_{0.20}Co_{0.08}O_2$ powders was undertaken and the effect of the nature of fuel and the annealing temperature on the thermodynamics, thermal, elemental, and structural properties of the materials were systematically analysed. The thermodynamic consideration of the combustion reaction shows that as the amount of citric acid fuel reduced and the amount of ammonium acetate increased the fuel-to-oxidiser molar ratio increased; while the heat of formation of products and the amount of gas produced reduced. The thermal analysis of the precursor gels containing varying compositions of the fuel(s) and metal nitrates showed that the 100% citric acid composition (100-T) produced the largest mass losses while the 50% citric acid composition (5050-T) produced the least. These mass losses were correlated with the enthalpy of the combustion reactions as modelled from the thermodynamic considerations. Unlike other reports in literature, it was shown that the citric acid fuel with a higher value of heat of combustion initiated the combustion reaction (exothermic decomposition) at a much higher temperature compared to the fuels with lower heat of combustion values. The elemental analysis of the samples revealed that reduction in the amount of citric acid fuels and increase in annealing temperature resulted in the loss of metals. The elemental analysis results also show that the usual practice of adding excess Li during synthesis of LLO and NCM layered oxides to compensate for Li loss during annealing should be further investigated in terms of the influence of temperature on it and its influence on the amounts of transition metals. The $Li_{1.20}Mn_{0.52}Ni_{0.20}Co_{0.08}O_2$ powders showed monoclinic C2/m structures based on Rietveld analysis. The annealing temperature greatly influenced the lattice parameters, unit cell volumes, crystallite sizes, and cationic disorder of the samples whilst the nature of fuel had little effect. The electrochemical performances of the $Li_{1.20}Mn_{0.52}Ni_{0.20}Co_{0.08}O_2$ powders used as cathode materials in LIB were also measured. Overall, the 100-T cathodes gave the best electrochemical performance compared to the 7525-T and 5050-T cathodes which was attributed to its better structural parameters. The results show that while the annealing temperature could be used to optimize the structural and electrochemical performance of the $Li_{1.20}Mn_{0.52}Ni_{0.20}Co_{0.08}O_2$ materials, the mixture of fuel (introduction of ammonium acetate) is not necessary.

Declaration of competing interest

The authors declare that they have no known competing financial interests or personal relationships that could have appeared to influence the work reported in this paper.

Acknowledgments

The Alexander von Humboldt Foundation Renewed Research Stay Fellowship and the assistance of the technical staff of IAM-ESS, Karlsruhe Institute of Technology, Germany are deeply appreciated.

Appendix A. Supplementary data

Supplementary data to this article can be found online at https://doi.org/10.1016/j.ceramint.2021.10.009.

References

[1] J.M. Tarascon, Key challenges in future Li-battery research, Philos. Trans. R. Soc. A. 368.1923 (2010) 3227–3241, https://doi.org/10.1098/rsta.2010.0112.
[2] J.M. Tarascon, M. Armand, Issues and challenges facing rechargeable lithium batteries. In materials for sustainable energy: a collection of peer-reviewed research and review articles, Nature (2011) 171–179, https://doi.org/10.1142/9789814317665_0024.
[3] N. Nitta, F. Wu, J.T. Lee, G. Yushin, Li-ion battery materials: present and future, Mater. Today 18 (2015) 252–264, https://doi.org/10.1016/j.mattod.2014.10.040.
[4] H. He, L. Zan, J. Liu, Y. Zhang, Template-assisted molten-salt synthesis of hierarchical lithium-rich layered oxide nanowires as high-rate and long-cycling cathode materials, Electrochim. Acta 333 (2020) 135558, https://doi.org/10.1016/j.electacta.2019.135558.
[5] L. Riekehr, J. Liu, B. Schwarz, F. Sigel, I. Kerkamm, Y. Xia, H. Ehrenberg, Effect of pristine nanostructure on first cycle electrochemical characteristics of lithium-rich lithium–nickel–cobalt–manganese-oxide cathode ceramics for lithium ion batteries, J. Power Sources 306 (2016) 135–147, https://doi.org/10.1016/j.jpowsour.2015.11.082.
[6] C.O. Ehi-Eromosele, S. Indris, G. Melinte, T. Bergfeldt, H. Ehrenberg, Solution combustion-mechanochemical syntheses of composites and core-shell cathode materials for lithium-ion batteries, ACS Sustain. Chem. Eng. 8 (2020) 18590–18605, https://doi.org/10.1021/acssuschemeng.0c06804.
[7] J. Li, J. Li, T. Yu, F. Ding, G. Xu, Z. Li, Y. Zhao, F. Kang, Stabilizing the structure and suppressing the voltage decay of Li $[Li_{0.2}Mn_{0.54}Co_{0.13}Ni_{0.13}]O_2$ cathode materials for Li-ion batteries via multifunctional Pr oxide surface modification, Ceram. Int. 42 (2016) 18620–18630, https://doi.org/10.1016/j.ceramint.2016.08.206.
[8] F. Wu, N. Li, Y. Su, L. Zhang, L. Bao, J. Wang, L. Chen, Y. Zheng, L. Dai, J. Peng, S. Chen, Ultrathin spinel membrane-encapsulated layered lithium-rich cathode material for advanced Li-ion batteries, Nano Lett. 14 (2014) 3550–3555, https://doi.org/10.1021/nl501164y.
[9] B. Xiao, B. Wang, J. Liu, K. Kaliyappan, Q. Sun, Y. Liu, G. Dadheech, M.P. Balogh, L. Yang, T.K. Sham, R. Li, Highly stable $Li_{1.2}Mn_{0.54}Co_{0.13}Ni_{0.13}O_2$ enabled by novel atomic layer deposited $AlPO_4$ coating, Nano Energy 34 (2017) 120–130, https://doi.org/10.1016/j.nanoen.2017.02.015.
[10] J. Zheng, X. Wu, Y. Yang, Improved electrochemical performance of $Li[Li_{0.2}Mn_{0.54}Ni_{0.13}Co_{0.13}]O_2$ cathode material by fluorine incorporation, Electrochim. Acta 105 (2013) 200–208, https://doi.org/10.1016/j.electacta.2013.04.150.
[11] D. Liu, X. Fan, Z. Li, T. Liu, M. Sun, C. Qian, M. Ling, Y. Liu, C. Liang, A cation/anion co-doped $Li_{1.12}Na_{0.08}Ni_{0.2}Mn_{0.6}O_{1.9}5F_{0.05}$ cathode for lithium ion batteries, Nano Energy 58 (2019) 786–796, https://doi.org/10.1016/j.nanoen.2019.01.080.
[12] C.O. Ehi-Eromosele, S. Indris, N.N. Bramnik, A. Sarapulova, V. Trouillet, L. Pfaffman, G. Melinte, S. Mangold, M.S.D. Darma, M. Knapp, H. Ehrenberg, In situ x-ray diffraction and x-ray absorption spectroscopic studies of a lithium-rich layered positive electrode material: comparison of composite and core–shell structures, ACS Appl. Mater. Interfaces 12 (2020) 13852–13868, https://doi.org/10.1021/acsami.9b21061.
[13] J.K. Noh, S. Kim, H. Kim, W. Choi, W. Chang, D. Byun, B.W. Cho, K.Y. Chung, Mechanochemical synthesis of Li_2MnO_3 shell/$LiMO_2$ (M= Ni, Co, Mn) core-structured nanocomposites for lithium-ion batteries, Sci. Rep. 4 (2014) 4847, https://doi.org/10.1038/srep04847.
[14] Z. J. Yang, F. Cheng, X. Zhang, H. Gao, Z. Tao, J. Chen, Porous $0.2Li_2MnO_3{\cdot}0.8LiNi_{0.5}Mn_{0.5}O_2$ nanorods as cathode materials for lithium-ion batteries J. Mater. Chem. A. 2 (2014) 1636–1640, https://doi.org/10.1039/C3TA14228K.
[15] H. He, H. Cong, Y. Sun, L. Zan, Y. Zhang, Spinel-layered integrate structured nanorods with both high capacity and superior high-rate capability as cathode material for lithium-ion batteries, Nano Res. 10 (2017) 556–569, https://doi.org/10.1007/s12274-016-1314-4.
[16] N.H. Vu, P. Arunkumar, J.C. Im, D.T. Ngo, H.T.T. Le, C.J. Park, W.B. Im, Effect of synthesis temperature on the structural defects of integrated spinel-layered $Li_{1.2}Mn_{0.75}Ni_{0.25}O_{2+\delta}$: a strategy to develop high-capacity cathode materials for Li-ion batteries, J. Mater. Chem. A. 5 (2017) 15730, https://doi.org/10.1039/C7TA04002D.
[17] F. Nomura, Y. Liu, T. Tanabe, N. Tamura, T. Tsuda, T. Hagiwara, T. Gunji, T. Ohsaka, F. Matsumoto, Optimization of calcination temperature in preparation of a high capacity Li-rich solid-solution $Li[Li_{0.2}Ni_{0.18}Co_{0.03}Mn_{0.58}]O_2$ material and its cathode performance in lithium ion battery, Electrochim. Acta 269 (2018) 321–330, https://doi.org/10.1016/j.electacta.2018.03.027.
[18] L. Huang, L. Liu, H. Wu, Y. Wang, H. Liu, Y. Zhang, Optimization of synthesis parameters for uniform sphere-like $Li_{1.2}Mn_{0.54}Ni_{0.13}Co_{0.13}O_2$ as high performance cathode material for lithium ion batteries, J. Alloys Compd. 775 (2019) 921–930, https://doi.org/10.1016/j.jallcom.2018.10.173.
[19] Q. Liu, H. Zhu, J. Liu, X. Liao, Z. Tang, C. Zhou, M. Yuan, J. Duan, L. Li, Z. Chen, High-performance lithium-rich layered oxide material: effects of preparation methods on microstructure and electrochemical properties, Materials 13 (2020) 334, https://doi.org/10.3390/ma13020334.
[20] Q. Jiang, K. Du, Y. He, A novel method for preparation of $LiNi_{1/3}Mn_{1/3}Co_{1/3}O_2$ cathode material for Li-ion batteries, Electrochim. Acta 107 (2013) 133–138, https://doi.org/10.1016/j.electacta.2013.05.148.
[21] Q. Ma, R. Li, R. Zheng, Y. Liu, H. Huo, C. Dai, Improving rate capability and decelerating voltage decay of Li-rich layered oxide cathodes via selenium doping to stabilize oxygen, J. Power Sources 331 (2016) 112–121, https://doi.org/10.1016/j.jpowsour.2016.08.137.
[22] M.N. Ates, S. Mukerjee, K.M. Abraham, A high rate Li-rich layered MNC cathode material for lithium-ion batteries, RSC Adv. 5 (2015) 27375–27386, https://doi.org/10.1039/C4RA17235C.
[23] K.R. Prakasha, A.S. Prakash, A time and energy conserving solution combustion synthesis of nano $Li_{1.2}Ni_{0.13}Mn_{0.54}Co_{0.13}O_2$ cathode material and its performance in Li-ion batteries, RSC Adv. 5 (2015) 94411–94417, https://doi.org/10.1039/C5RA19096G.

[24] V. Mathew, B. Sambandam, S. Kim, S. Kim, S. Park, S. Lee, J. Lee, S. Park, J. Song, J. Kim, High-voltage cathode materials by combustion-based preparative approaches for Li-ion batteries application, J. Power Sources 472 (2020) 228368, https://doi.org/10.1016/j.jpowsour.2020.228368.

[25] C.O. Ehi-Eromosele, S.O. Ajayi, C.N. Onwucha, Optimizing the electrochemical performance of Li_2MnO_3 cathode materials for Li-ion Battery using solution combustion synthesis: higher and longer temperature syntheses improves performance, J. Alloys Compd. 861 (2021) 157972, https://doi.org/10.1016/j.jallcom.2020.157972.

[26] C.O. Ehi-Eromosele, S.O. Ajayi, C.N. Onwucha, Influence of fuels in the sol-gel combustion synthesis of Li_2MnO_3 positive electrode material for Li-ion battery, Mater. Chem. Phys. (2020) 124055, https://doi.org/10.1016/j.matchemphys.2020.124055.

[27] S.H. Kang, P. Kempgens, S. Greenbaum, A.J. Kropf, K. Amine, M.M. Thackeray, Interpreting the structural and electrochemical complexity of $0.5Li_2MnO_3{\cdot}0.5LiMO_2$ electrodes for lithium batteries (M= $Mn_{0.5-x}Ni_{0.5-x}Co_{2x}$, $0 \leq x \leq 0.5$), J. Mater. Chem. 17 (20) (2007) 2069–2077, https://doi.org/10.1039/B618715C.

[28] C.O. Ehi-Eromosele, B. I Ita, E.E.J. Iweala, Synthesis, microstructure and magnetic properties of nanocrystalline $MgFe_2O_4$ particles: effect of mixture of fuels and sintering temperature, Sci. Sinter. 48 (2016) 221–235, https://doi.org/10.2298/SOS1602221O.

[29] A.B. Salunkhe, V.M. Khot, M.R. Phadatare, S.H. Pawar, Combustion synthesis of cobalt ferrite nanoparticles—influence of fuel to oxidizer ratio, J. Alloys Compd. 514 (2012) 91–96, https://doi.org/10.1016/j.jallcom.2011.10.094.

[30] J.A. Dean, Lange's Handbook of Chemistry, vol. 15, McGraw-Hill, Newyork, 1992.

[31] R.K. Lenka, T. Mahata, P.K. Sinha, A.K. Tyagi, Combustion synthesis of gadolinia-doped ceria using glycine and urea fuels, J. Alloys Compd. 466 (2008) 326–329, https://doi.org/10.1016/j.jallcom.2007.11.028.

[32] Y. Chen, S. Luo, J. Leng, S. Deng, S. Yan, X. Tian, Y. Li, J. Guo, T. Lei, J. Zheng, Exploring the synthesis conditions and formation mechanisms of Li-rich layered oxides via solid-state method, J. Alloys Compd. (2020) 157204, https://doi.org/10.1016/j.jallcom.2020.157204.

[33] C.C. Wang, K.A. Jarvis, P. J Ferreira, A. Manthiram, Effect of synthesis conditions on the first charge and reversible capacities of lithium-rich layered oxide cathodes, Chem. Mater. 25 (2013) 3267–3275, https://doi.org/10.1021/cm402181f.

[34] A.K. Shukla, Q.M. Ramasse, C. Ophus, D.M. Kepaptsoglou, F.S. Hage, C. Gammer, C. Bowling, P.A.H. Gallegos, S. Venkatachalam, Effect of composition on the structure of lithium-and manganese-rich transition metal oxides, Energy Environ. Sci. 11 (2018) 830–840, https://doi.org/10.1039/C7EE02443F.

[35] M.M. Thackeray, S.H. Kang, C.S. Johnson, J.T. Vaughey, R. Benedek, S.A. Hackney, Li_2MnO_3-stabilized $LiMO_2$ (M= Mn, Ni, Co) electrodes for lithium-ion batteries, J. Mater. Chem. 17 (2007) 3112–3125, https://doi.org/10.1039/B702425H.

[36] J. Li, J. Camardese, R. Shunmugasundaram, S. Glazier, Z. Lu, J.R. Dahn, Synthesis and characterization of the lithium-rich core–shell cathodes with low irreversible capacity and mitigated voltage fade, Chem. Mater. 27 (2015) 3366–3377, https://doi.org/10.1021/acs.chemmater.5b00617.

[37] S. Kim, C. Kim, Y.I. Jhon, J.K. Noh, S.H. Vemuri, R. Smith, K.Y. Chung, M.S. Jhon, B.W. Cho, Synthesis of layered−layered $0.5Li_2MnO_3{\cdot}0.5LiCoO_2$ nanocomposite electrode materials by the mechanochemical process and first principles study, J. Mater. Chem. 22 (2012) 25418–25426, https://doi.org/10.1039/C2JM35654F.

[38] L. Xu, J. Meng, P. Yang, H. Xu, S. Zhang, Enhanced electrochemical performance of lithium-rich layered oxide cathodes by a facile self-template method for lithium-ion batteries, Solid State Ionics 348 (2020) 115281, https://doi.org/10.1016/j.ssi.2020.115281.

[39] X. Xiang, W. Li, Significant influence of insufficient lithium on electrochemical performance of lithium-rich layered oxide cathodes for lithium ion batteries, Electrochim. Acta 133 (2014) 422–427, https://doi.org/10.1016/j.electacta.2014.04.084.

[40] R.E. Ruther, H. Dixit, A.M. Pezeshki, R.L. Sacci, V.R. Cooper, J. Nanda, G. M, Veith, Correlating local structure with electrochemical activity in Li_2MnO_3, J. Phys. Chem. 119 (2015) 18022–18029, https://doi.org/10.1021/acs.jpcc.5b03900.

[41] P.K. Nayak, J. Grinblat, M. Levi, E. Levi, S. Kim, J.W. Choi, D. Aurbach, Al doping for mitigating the capacity fading and voltage decay of layered Li and Mn-rich cathodes for Li-ion batteries, Adv. Energy Mater. 6 (2016) 1502398, https://doi.org/10.1002/aenm.201502398.

[42] J. Liu, H. Chen, J. Xie, Z. Sun, N. Wu, B. Wu, Electrochemical performance studies of Li-rich cathode materials with different primary particle sizes, J. Power Sources 251 (2014) 208–214, https://doi.org/10.1016/j.jpowsour.2013.11.055.

[43] C.R. Fell, D. Qian, K.J. Carroll, M. Chi, J. L Jones, Y.S. Meng, Correlation between oxygen vacancy, microstrain, and cation distribution in lithium-excess layered oxides during the first electrochemical cycle, Chem. Mater. 25 (9) (2013) 1621–1629, https://doi.org/10.1021/cm4000119.